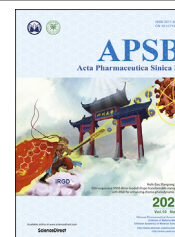




Chinese Pharmaceutical Association
Institute of Materia Medica, Chinese Academy of Medical Sciences

Acta Pharmaceutica Sinica B

www.elsevier.com/locate/apsb
www.sciencedirect.com



ORIGINAL ARTICLE

GSH-responsive SN38 dimer-loaded shape-transformable nanoparticles with iRGD for enhancing chemo-photodynamic therapy



Congcong Lin^{a,b,†}, Fan Tong^{c,†}, Rui Liu^c, Rou Xie^c, Ting Lei^c,
Yuxiu Chen^c, Zhihang Yang^c, Huile Gao^{c,*}, Xiangrong Yu^{a,*}

^aDepartment of Radiology, Zhuhai People's Hospital, Jinan University, Zhuhai 519000, China

^bDepartment of Medicinal Chemistry and Natural Medicine Chemistry, College of Pharmacy, Harbin Medical University, Harbin 150081, China

^cKey Laboratory of Drug Targeting and Drug Delivery Systems, West China School of Pharmacy, Sichuan University, Sichuan 610041, China

Received 26 July 2020; received in revised form 12 September 2020; accepted 28 September 2020

KEY WORDS

Shape-transformable;
SN38 dimer;
GSH-responsive;
Chemo-photodynamic
therapy;
iRGD;
Co-administration;
Ce6;
Breast cancer

Abstract Accurate tumor targeting, deep penetration and superb retention are still the main pursuit of developing excellent nanomedicine. To achieve these requirements, a stepwise stimuli-responsive strategy was developed through co-administration tumor penetration peptide iRGD with shape-transformable and GSH-responsive SN38-dimer (d-SN38)-loaded nanoparticles (d-SN38@NPs/iRGD). Upon intravenous injection, d-SN38@NPs with high drug loading efficiency ($33.92 \pm 1.33\%$) could effectively accumulate and penetrate into the deep region of tumor sites with the assistance of iRGD. The gathered nanoparticles simultaneously transformed into nanofibers upon 650 nm laser irradiation at tumor sites so as to promote their retention in the tumor and burst release of reactive oxygen species for photodynamic therapy. The loaded d-SN38 with disulfide bond responded to the high level of GSH in tumor cytoplasm, which consequently resulted in SN38 release and excellent chemo-photodynamic effect on tumor. *In vitro*, co-administering iRGD with d-SN38@NPs+laser showed higher cellular uptake, apoptosis ratio and

*Corresponding authors. Tel./fax: +86 28 85502532.

E-mail addresses: gaohuile@scu.edu.cn (Huile Gao), yxr00125040@126.com (Xiangrong Yu).

[†]These authors made equal contributions to this work.

Peer review under responsibility of Institute of Materia Medica, Chinese Academy of Medical Sciences and Chinese Pharmaceutical Association.

<https://doi.org/10.1016/j.apsb.2020.10.009>

2211-3835 © 2020 Chinese Pharmaceutical Association and Institute of Materia Medica, Chinese Academy of Medical Sciences. Production and hosting by Elsevier B.V. This is an open access article under the CC BY-NC-ND license (<http://creativecommons.org/licenses/by-nc-nd/4.0/>).

multicellular spheroid penetration. *In vivo*, d-SN38@NPs/iRGD+laser displayed advanced penetration and accumulation in tumor, leading to 60.89% of tumor suppression in 4T1 tumor-bearing mouse model with a favorable toxicity profile. Our new strategy combining iRGD with structural transformable nanoparticles greatly improves tumor targeting, penetrating and retention, and empowers anticancer efficacy.

© 2020 Chinese Pharmaceutical Association and Institute of Materia Medica, Chinese Academy of Medical Sciences. Production and hosting by Elsevier B.V. This is an open access article under the CC BY-NC-ND license (<http://creativecommons.org/licenses/by-nc-nd/4.0/>).

1. Introduction

Progress in developing effective nanomedicines has been impeded by heterogeneity of the enhanced permeability and retention (EPR) effect in different tumor type, location and mass size^{1–4}. The tumor permeability and retention of nanocarriers are not only related to their size, but also closely associated with their shape and chemistry surface^{5–8}. However, it is worth noting that permeability and retention in “static” nanoparticles are often mutual contradictory^{9,10}. To address the dilemma and compensate the poor EPR efficacy, shape transformable nanoparticles that can achieve *in situ* morphology change have attracted our attention^{11–15}. Typically, the nanosphere offers the vehicle a proper stability to circulate and distribute to the tumor, while the nanofiber confers it a superb retention capability around and inside tumor^{7,16,17}. In light of this, convertible nanocarriers that can transform the morphology of nanospheres into nanofibers may fuel the nanotherapy outcomes.

Recently, transformable linear chimeric triblock molecules Ce6/BR-FFVLK-PEG were designed by our lab¹⁸. The hydrophobic head [chlorin e6 (Ce6) or bilirubin (BR)], and hydrophilic tail [polyethylene glycol (PEG)] were tandem conjugated with Phe-Phe-Val-Leu-Lys (FFVLK) for forming spherical micelles. Notably, the formulation remained in spherical when circulated and distributed into the tumor. Upon the controllable 650 nm laser irradiation at tumor site, (1) the photosensitizer Ce6 was activated and reactive oxygen species (ROS) were generated for photodynamic therapy (PDT); (2) the strong and stable intermolecular forces of the micelles were broken^{19,20}. Subsequently, spherical nanoparticles were transformed into nanofibers, which markedly facilitate their retention inside the tumor. However, to enlarge the therapeutic potency upon PDT, it is still necessary to combine with other strategies. On the other hand, the accumulation of this shape-transformable formulation in the tumor site mainly depended on the passive EPR effect, resulting in relatively low targeting efficacy²¹. Active targeting provides a noteworthy additional benefit for high tumor location, which is the premise for nanomedicine to play the designed role^{22,23}. In this context, constructing an actively targeted shape-transformable nanomedicine for combinational therapy is a feasible strategy to maximize the treatment outcome.

Mounting studies have shown that the combination of PDT and chemotherapy, namely chemo-photodynamic therapy, can increase susceptibility of tumor cells towards chemotherapeutics, thus producing better synergistic antitumor effect^{19,24–26}. To achieve the goal of chemo-photodynamic therapy, the chemotherapeutics should be released with locally confined treatment modalities. Additionally, stimuli-responsive drug release at the right place and right time plays a paramount role for reducing systemic toxicity of chemotherapeutics. Equipped with various responsive bonds to stimuli, including redox, pH, enzyme, light and temperature,

dimeric prodrug has emerged as one of the most promising strategies to fulfill the requirement of on-demand drug release^{27–30}. Moreover, it has documented that dimeric prodrugs can also help to address the low drug loading efficiency in amphiphilic copolymers by increasing intermolecular hydrophobic interaction between molecules^{31,32}. 7-Ethyl-10-hydroxy camptothecin (SN38), the biologically active metabolite of irinotecan (CPT-11), has proven to be approximately 1000-fold more cytotoxic than CPT-11 by inhibiting DNA topoisomerase^{33,34}. The relatively high toxicology as well as the unfavorable pharmacology of SN38 limited its direct application^{35,36}. In this perspective, SN38 dimer (d-SN38) linked *via* disulfide bond was synthesized and selected as the payload. The disulfide bond of d-SN38 was stable in bloodstream but can be efficiently cleaved by intracellular thiols, such as the high level of glutathione (GSH) in cytoplasm of tumor cells^{37,38}. Therefore, loading d-SN38 in the above shape-transformable nanocarrier is capable to attain a better antitumor effect.

To endow active targeting property to the formulation, targeting ligands were widely utilized due to their specific interaction with receptors that overexpressed in tumor. However, the modification of particles with ligand makes the preparation complex, and it may influence the responsiveness^{14,39}. Therefore, co-injection particles with targeting enhancer are a promising strategy. iRGD (cRGDKGPDC), a widely used targeting enhancer with tumor-penetrating capacity, homes to tumors by initially binding to $\alpha v \beta 3$ integrin receptors that are specifically expressed in tumor vessels and tumor cells⁴⁰. Subsequently, a C-end rule motif with specific affinity with neuropilin-1 (NRP-1) is produced through proteolytic cleavage^{41,42}. When co-administered with drug or nanoparticles, iRGD can facilitate the penetration into extravascular tumor tissue⁴³. This co-administration strategy provides a versatile way to greatly simplify the path to clinical application. As such, we utilized the active tumor-specific tissue penetration feature conferred on iRGD to enhance cancer targeted drug delivery by co-injection.

Herein, to boost the tumor targeting, penetration and retention, we established a stepwise multiple stimuli-responsive strategy through co-administration iRGD with GSH-responsive SN38 dimer-loaded shape-transformable Ce6/BR-FFVLK-PEG micelles (d-SN38@NPs/iRGD) for chemo-photodynamic therapy of breast cancer (Scheme 1). The particle size, entrapment efficiency, GSH responsiveness, stability and drug release properties of d-SN38@NPs were characterized. Cellular uptake and cytotoxicity by the d-SN38@NPs/iRGD combined with PDT (d-SN38@NPs/iRGD+laser) were evaluated in mouse breast cancer 4T1 cells by both quantitative and qualitative methods. Their targeting and antitumor efficacies in tumor-bearing mice were determined by *in vivo* imaging and tumor growth curve. Overall, d-SN38@NPs/iRGD+laser showed superior tumor-targeting efficiency and excellent therapeutic effects.

2. Materials and methods

2.1. Materials

iRGD and FFVLK-(PEG8)₃ (MW = 1923.2 Da) were synthesized by Shanghai Dechi Biosciences Co., Ltd. (Shanghai, China). Ce6 was purchased from Dalian Meilun Biotech Co., Ltd. (Dalian, China). Bilirubin was gained from Tokyo Chemical Industry Co., Ltd. (Tokyo, Japan). d-SN38 was supplied by Prof. Jun Cao (Sichuan University, China). 4',6-Diamidino-2-phenylindole (DAPI) and LysoTracker green was purchased from Life Technologies (Grand Island, USA). FITC Annexin V Apoptosis Detection Kit I was obtained from BD Pharmingen™ (Franklin Lakes, NJ, USA). Calcein-AM/PI Double Stain Kit was supplied by Yeasen (Shanghai, China). 24-well hanging cell culture inserts (8.0 μm, PET) were obtained from Corning Inc. (Kennebunk, ME, USA). All other reagents and solvents were purchased from commercial resources and used without further purification unless otherwise noted. Mouse mammary breast tumor cell line 4T1 was obtained from Chinese Academy of Sciences Cells Bank (Shanghai, China). 4T1 cells were incubated in RPMI-1640 cell culture medium supplemented with 10% fetal bovine serum (FBS) and 100 U/mL streptomycin, and 100 U/mL penicillin at 37 °C in a humidified 5% CO₂ atmosphere.

2.2. Animals

Female BALB/c mice (5–6 weeks, 18 ± 2 g) and nude mice (4–5 weeks, 18 ± 2 g) were supplied by Dashuo Biotechnology Co., Ltd. (Chengdu, China). All animal experiments were conducted according to the guidelines of the Ethics Committee of Sichuan University, Chengdu, China.

2.3. Preparation and characterization of d-SN38@NPs

Ce6-FFVLK-PEG and BR-FFVLK-PEG were synthesized and a molar ratio of 1:1 Ce6/BR was chosen for NPs preparation with

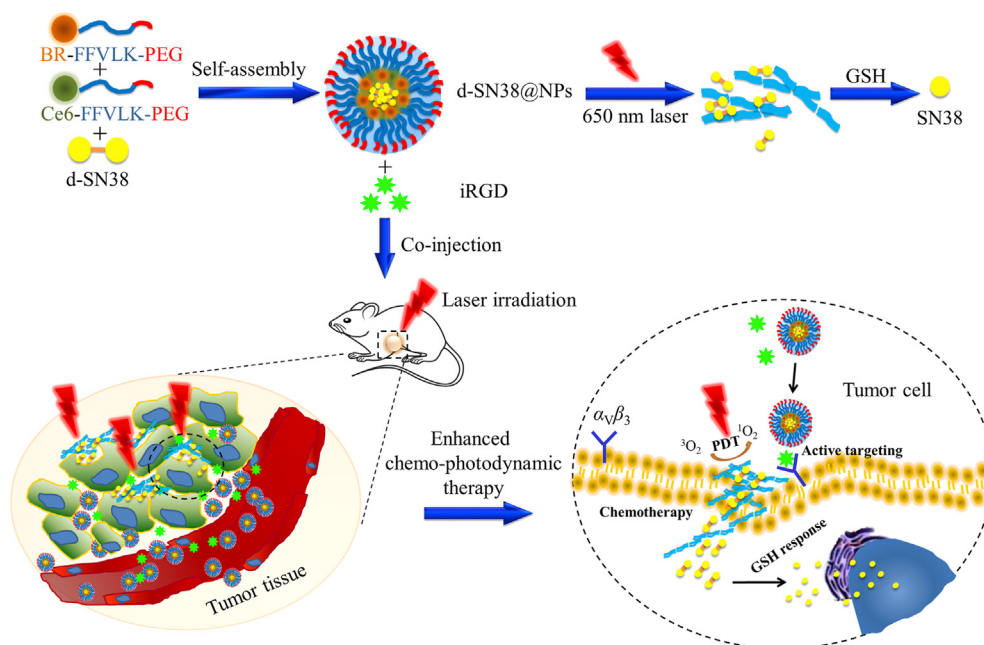
notable and sensitive morphological change ability of nanofibers according to our previously report¹⁸. The Ce6-FFVLK-PEG and BR-FFVLK-PEG were dissolved in chloroform (0.3 mL) and mixed with d-SN38 solution (4 mg in 0.1 mL of chloroform). Then the mixture was added into ultrapure water (7 mL) and subsequently emulsified using ultrasonic cell crusher (65 W, 5 s/5 s a cycle for 5 min). The suspension was transferred into rotary evaporation to remove chloroform, yielding uniform-sized d-SN38@NPs. The same procedure was followed to prepare blank nanoparticle (NPs) without d-SN38.

The size and morphology changes of d-SN38@NPs before and after receiving 650 nm laser irradiation (200 mW/cm² for 5 min, the same below unless otherwise stated) were monitored by dynamic light scattering (DLS, Malvern Panalytical, Malvern Zetasizer Nano ZS, Malvern, UK) and measured by transmission electronic microscopy (TEM, Hitachi, H-600, Tokyo, Japan). For stability evaluation, d-SN38@NPs was incubated in medium containing 10% and 50% FBS at different temperatures (37, 25 and 4 °C) and pH values (7.4 and 6.5). The size changes were monitored for 24 h by DLS. Besides, to confirm the responsiveness of d-SN38 to GSH in tumor cytoplasm, d-SN38 was incubated with GSH at 10 × 10⁻³ mol/L, and the fluorescence spectrum change was detected by spectrofluorophotometer (Shimadzu, RF-5301PC, Tokyo, Japan) at 1, 2, 4 and 8 h.

The free drug was removed by centrifugal filters (10 K MWCO, Millipore Corp, Milli-Q, Billerica, MA, USA), then concentration of d-SN38 in particles was determined with microplate reader (Thermo Scientific, Varioskan Flash, Waltham, MA, USA) at Ex/Em of 375 nm/427 nm. The encapsulation efficiency and loading capacity were obtained according to the following Eqs. (1) and (2):

Encapsulation

$$\text{efficiency}(\%) = \frac{\text{Weight of drug contained in nanoparticles}}{\text{Weight of total drug}} \times 100 \quad (1)$$



Scheme 1 The schematic illustration of the preparation, drug delivery and tumor response of d-SN38@NPs/iRGD.

Loading

$$\text{capacity}(\%) = \frac{\text{Weight of drug contained in nanoparticles}}{\text{Weight of nanoparticles} \times 100} \quad (2)$$

2.4. *In vitro* release of d-SN38@NPs

For *in vitro* release study of d-SN38@NPs, d-SN38@NPs (0.7 mL, 1 mg/mL) receiving irradiation or not were resuspended in PBS (7 mL) containing 0.5% Tween 80 at pH 7.4 or pH 6.5 respectively, then dialyzed for 48 h under 37 °C. 1 mL of release medium was taken out in each sample at 0.5, 1, 2, 4, 8, 12, 24 and 48 h, while an equal volume of fresh media was supplemented at certain time intervals. The fluorescent intensity of d-SN38 from different formulations in pH values 7.4 and 6.5 were determined at different time points.

2.5. ROS generation

4T1 cells were seeded at a density of 1×10^5 cells per well in 6-well plates. After grown to 80% confluent, NPs, d-SN38@NPs and d-SN38@NPs/iRGD were added into the wells at the same Ce6 concentration (5 µg/mL) for 2 h, respectively. The cells treated with PBS were set as negative control. After receiving 650 nm irradiation for 2 min, the ROS level was tested by ROS Assay Kit (10 µmol/L DCFH-DA, 35 min). Then the cells were washed, fixed and imaged by confocal laser scanning microscope (CLSM, Olympus, FV1000, Central Valley, PA, USA).

2.6. Cellular uptake

4T1 cells were inoculated at a density of 3×10^5 in a confocal dish (35 mm × 10 mm) and grown for 24 h. Thereafter, NPs and NPs/iRGD were added into the wells at the same Ce6 concentration (5 µg/mL), respectively. The concentration of iRGD was 43.3 µg/mL in NPs/iRGD group. One hour later, part of NPs- and NPs/iRGD-treated cells were carried out to receive 650 nm irradiation for 2 min. All treatment groups were maintained for another 1 h, then washed with cold PBS and fixed with 4% paraformaldehyde. To stain nuclei, the cells were incubated with 0.5 µg/mL of DAPI for 5 min. Finally, the cells were imaged by CLSM (Olympus).

For quantitative studies, 4T1 cells were seeded in 6-well plates at a density of 3×10^5 cells per well. After 24 h, different formulations were added to the plates and the cells were treated as described above. After 2 h incubation, the cells were harvested. The fluorescence intensity of Ce6 was detected by flow cytometry (Beckman Coulter, FC500, Brea, CA, USA).

2.7. Penetration and retention in multicellular spheroid

To prepare multicellular spheroids, 4T1 cells (1×10^3 cells per well) were seeded in 2% (w/v) low-melting point agarose coated 96-well plates⁴⁴. After seven days, the compacted and uniform spheroids were selected for penetration study. The tumor spheroids were transferred to a confocal dish and incubated with NPs and NPs/iRGD at an equivalent concentration of Ce6 (5 µg/mL), respectively. Four hours later, part of spheroids was taken out to receive 650 nm irradiation for 2 min. All spheroids were maintained for another 2 h, and then the spheroids were rinsed and fixed. Z-stack images of spheroids from the top to 100 µm were collected using CLSM (Olympus).

2.8. Cytotoxicity study

Firstly, MTT assay was carried out to investigate the cytotoxicity of different formulations. 5×10^3 per well of 4T1 cells were plated and cultured in 96-well plates for 24 h. Ce6, d-SN38, NPs, d-SN38@NPs and d-SN38@NPs/iRGD were added into each well. The final concentrations of d-SN38 and Ce6 ranged from 0 to 15 and 2.5 µg/mL, respectively. The d-SN38@NPs/iRGD group was coincubated with iRGD from 0 to 129.9 µg/mL. In the laser irradiation group, cells were stimulated at 12 h after administration and then cultured for another 12 h. The cell viability of these formulations was examined by MTT⁴⁵.

Secondly, the cytotoxicity was evaluated by Calcein-AM/PI double stain method. In brief, 4T1 cells (1×10^5 per well) were grown in 24-well plates as above for 24 h. Free Ce6, free d-SN38, NPs, d-SN38@NPs and d-SN38@NPs/iRGD were added to each well with 0.1 µg/mL of Ce6, 0.5 µg/mL of d-SN38 and 4.33 µg/mL of iRGD correspondingly. After 4 h of culture, half of the cells received 650 nm irradiation for 2 min. Cells incubated with fresh culture medium was set as control. After another 4 h of incubation, the cells were washed and stained by Calcein-AM (5 µg/mL) and PI (10 µg/mL) for 30 min. Finally, the stained cells were imaged by fluorescent microscope (Shimadzu).

To assess the cell apoptosis induced by the architected formulations, 4T1 cells (5×10^4 per well) were plated in 12-well plates. The cells were treated with Ce6, d-SN38, NPs, d-SN38@NPs and d-SN38@NPs/iRGD followed by the same irradiation schedule as MTT assay. The concentrations of Ce6, d-SN38 and iRGD were 0.05, 0.25 and 2.165 µg/mL, respectively. After 24 h incubation, the cells were harvested and stained with Annexin V-FITC and PI. Finally, the cell apoptosis in different groups was analyzed by flow cytometer (Beckman Coulter)⁴⁶.

2.9. Wound healing assay

For wound healing assay, 5×10^5 4T1 cells were seeded in 12-well plates and incubated until 90% confluence. The confluent cell monolayers were wounded with a 10-µL pipette tip to get two cell islands, then washed and incubated with d-SN38@NPs or d-SN38@NPs/iRGD at a concentration of 0.25 µg/mL Ce6 for another 24 h. In the laser irradiation group, laser irradiation was given after 12 h. The wound healing area was photographed at the beginning (0 h) and 24 h with a microscope. The cell motility was calculated according to the following Eq. (3)⁴⁷:

$$\text{Cell motility}(\%) = \left(1 - \frac{\text{Wound width at 24 h}}{\text{Wound width at 0 h}}\right) \times 100 \quad (3)$$

2.10. Pharmacokinetics study

Female BALB/c mice ($n = 3$) were intravenously injected with d-SN38@NPs and d-SN38@NPs/iRGD at a dosage of 5 mg/kg of Ce6, respectively. 40 µL of blood sample was collected at 0.25, 0.5, 1, 2, 4, 8, 12, 24 and 48 h post injection. The Ce6 fluorescence signal (Ex 640 nm, Em 710 nm) of each sample was analyzed by Lumina III Imaging System (PerkinElmer, IVIS Lumina III, Waltham, MA, USA).

2.11. In vivo targeting efficiency

100 μL of 4T1 cells (2×10^5) were subcutaneously injected to the left mammary fat pads of female BALB/c nude mouse. 7 days later, mice with tumor around 100 mm^3 were randomly divided into three groups ($n = 3$). Two groups of mice were given d-SN38@NPs and d-SN38@NPs/iRGD, respectively. The last group of mice was intravenously administrated with d-SN38@NPs/iRGD, while the tumor sites of the mice were irradiated with 650 nm laser at 1 h before every imaging point. The fluorescence signal (Ex 640 nm, Em 710 nm) was determined at 4 and 24 h post-intravenous administration using Lumina III Imaging System (PerkinElmer). The mice were sacrificed by cervical dislocation after last imaging. Tumors and major tissues were collected, fixed, dehydrated and sliced for fluorescence study⁴⁸. After stained the nuclei with DAPI (0.5% $\mu\text{g}/\text{mL}$), images of the slices were captured by a confocal microscope (Olympus).

2.12. In vivo antitumor efficacy

Implantation of 4T1 cells was performed in BALB/c mice as described above. Mice with tumor around 100 mm^3 were randomized into five treatment groups and the control group that received saline ($n = 5$). The treatment groups were intravenously given NPs, d-SN38@NPs, d-SN38@NPs/iRGD, d-SN38@NPs+laser and d-SN38@NPs/iRGD+laser at a dose of d-SN38 10 mg/kg once every 3 days for a total of 4 times, while the dose of iRGD was 86.6 mg/kg in iRGD co-injection groups. Twenty four hours post administration, the laser groups received irradiation at tumor site (200 mW/cm^2 for 5 min). Tumor volume and body weight were recorded every 2 days. Mice were sacrificed one day after the last irradiation. Tumors and major organs were collected and sampled for hematoxylin and eosin (H&E) staining and TUNEL staining.

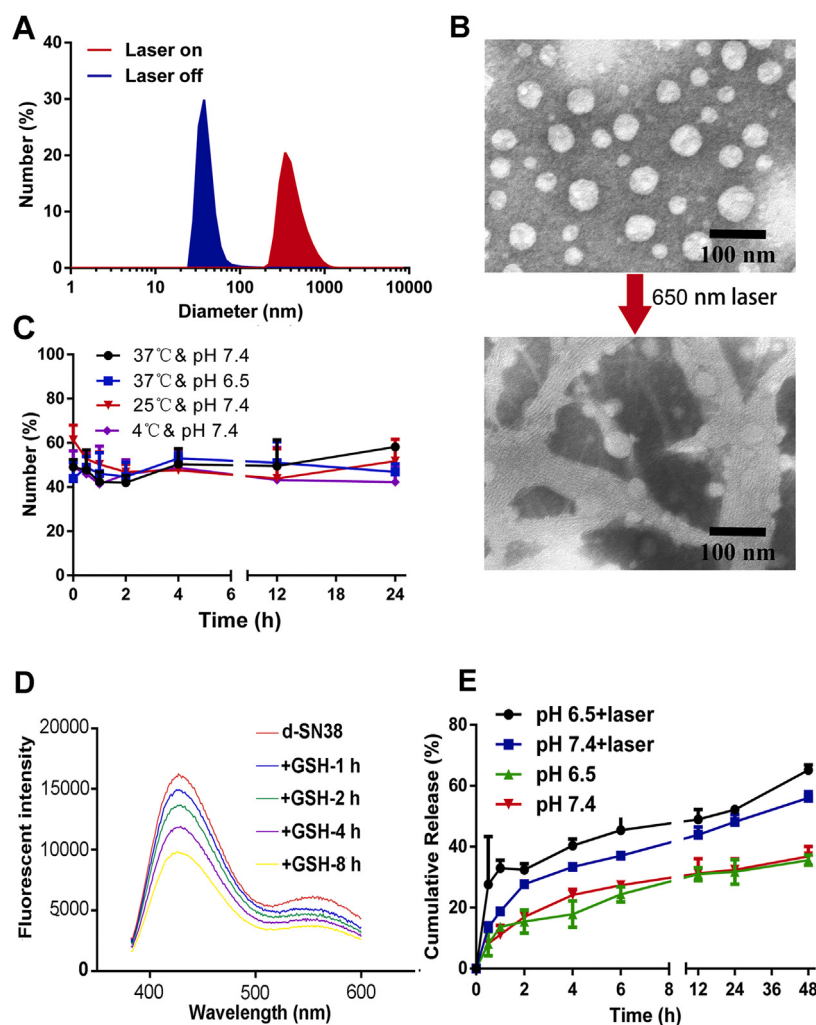


Figure 1 Characterization of d-SN38@NPs. (A) Size changes of d-SN38@NPs post 650 nm irradiation measured by DLS; (B) TEM image of d-SN38@NPs and d-SN38@NPs post 650 nm irradiation; (C) Stability of d-SN38@NPs in different pH conditions for 24 h ($n = 3$); (D) Fluorescence emission spectra changes of d-SN38 after incubating with GSH; (E) Drug release from d-SN38@NPs upon or not upon 650 nm irradiation in different pH medium ($n = 3$).

2.13. Statistical analysis

Mean \pm standard deviation (SD) values were used for data expression, unless specified otherwise. Statistical analyses were performed using Student's *t*-test and $P < 0.05$ was considered statistically significant.

3. Results and discussion

3.1. Characterization of d-SN38@NPs

The nanoparticles were formed by self-assembly of the two linear chimeric triblock molecules (Supporting Information Fig. S1), and d-SN38 was incorporated in the hydrophobic core through

hydrophobic interactions and the π - π stacking^{49,50}. The diameter of d-SN38@NPs was 46.62 ± 2.15 nm with a uniform dispersity. However, the size of d-SN38@NPs after receiving 650 nm laser irradiation apparently increased to 207.0 ± 4.3 nm (Fig. 1A). Furthermore, an extensive morphological change from sphere to nanofiber was observed by TEM (Fig. 1B). The notable size and morphology changes collectively suggested that the morphology transformable system was successfully prepared (Supporting Information Fig. S2); this structural transformable ability could endow d-SN38@NPs a superior retention property.

The hydrodynamic diameter of d-SN38@NPs showed no perceivable changes in different pH values (6.5 and 7.4) and different temperatures (4, 25 and 37 °C) with a stable size around 46 nm (Fig. 1C). Furthermore, the turbidity changes of d-SN38@NPs in

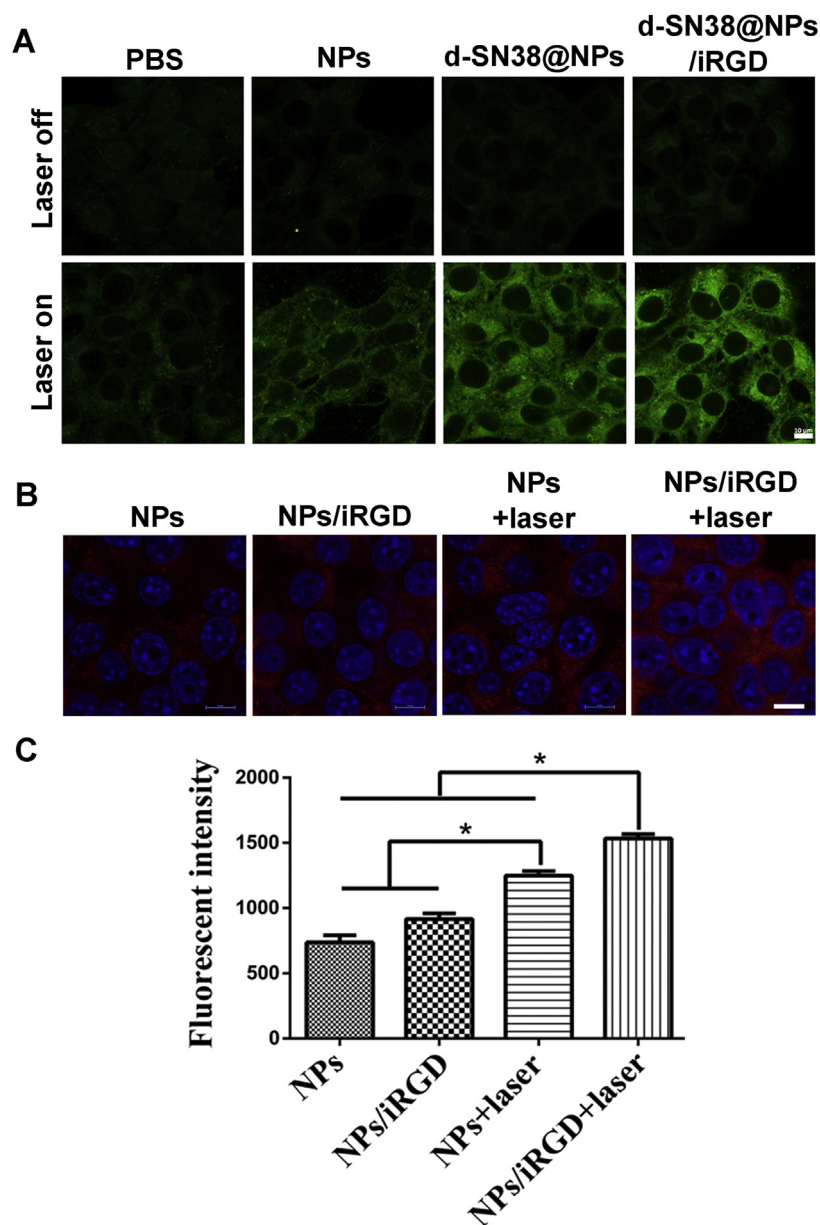


Figure 2 ROS generation and cellular uptake of various formulations. (A) ROS generation of PBS, NPs, d-SN38@NPs and d-SN38@NPs/iRGD upon 650 nm irradiation or not at cell level, scale bar = 10 μ m; (B) Cellular uptake of NPs and NPs/iRGD upon 650 nm irradiation or not using confocal microscope, scale bar = 10 μ m; (C) Flow cytometry analysis, error bars indicate SD ($n = 3$), * $P < 0.05$.

10% and 50% FBS were quantified with UV–Vis spectra by detecting the light transmittance and no obvious variations were observed after 24 h incubation (Supporting Information Fig. S3). Both results verified that d-SN38@NPs possessed excellent stability.

Due to the abnormal metabolism of tumor tissue, there is a strong reduction environment in tumor cells. The concentration of GSH in tumor cells is more than 1000 times higher than that in normal cells⁵¹. In order to maximize the accuracy of tumor targeted therapy, d-SN38 was designed to generate monomeric drug SN38 activity in tumor cells when released from nanoparticles. As shown in Fig. 1D, the fluorescence intensity of d-SN38 under the GSH-abundant circumstance extensively reduced with time, which verified the GSH responsiveness of the dimers. And as shown in Supporting Information Figs. S4 and S5, the chemical structures of SN38 and d-SN38 were further confirmed by NMR and IR. Besides, the reduced molecular rigidity of drug dimers makes it easier to incorporate in nanoparticles. In this composition, the drug loading content was $33.92 \pm 1.33\%$ with a proper encapsulation efficiency ($82.91 \pm 3.24\%$), which is more than 6-fold higher than that of most reported micellar systems (normally lower than 5%)⁵².

3.2. In vitro release of d-SN38@NPs

The release behaviors of d-SN38 from the nanoparticles were monitored using a dialysis method. As shown in Fig. 1E, post irradiation, approximately 30% of d-SN38 was burst released from d-SN38@NPs in pH 6.5 medium at the first 0.5 h, whereas that without irradiation was less than 10%. When the incubation medium came to pH 7.4, the release ratio slightly decreased in d-SN38@NPs upon irradiation group ($13.47 \pm 1.54\%$), which was also higher than that of laser off ($8.22 \pm 1.45\%$). After 48 h, the cumulative release of d-SN38@NPs upon irradiation at pH 6.5 and 7.4 were $65.14 \pm 1.67\%$ and $56.05 \pm 2.00\%$, respectively, and those without irradiation was $36.85 \pm 3.26\%$ and $35.59 \pm 1.65\%$, respectively. The highest cumulative release of d-SN38@NPs upon irradiation at pH 6.5 suggested that irradiation induced structural transformation as well as the acidic circumstance

promoted the drug release of d-SN38@NPs, which is also favorable for the efficient delivery of drug into tumor cells⁵³.

3.3. ROS generation

The ROS generation ability of different formulations on 4T1 cells was determined. As shown in Fig. 2A, without irradiation, almost no ROS was generated in all the formulations. However, upon irradiation, ROS signal significantly increased, demonstrating that NPs in tumor area can provide abundant ROS level. Interestingly, the ROS generated by d-SN38@NPs and d-SN38@NPs/iRGD was slightly higher than that of NPs. This result may attribute to the down-regulation of GSH by d-SN38, which reduced the consumption of ROS.

3.4. Cellular uptake

To investigate the cell penetration behavior of the prepared nanoparticle when co-administrated with iRGD, qualitative and quantitative cellular uptake studies were carried out in $\alpha v\beta 3$ and NRP-1 overexpressed 4T1 cells^{54,55}. The results of laser confocal fluorescence microscopy and flow cytometry showed that laser irradiation can effectively promote the uptake of d-SN38@NPs in 4T1 cells (Fig. 2B and C), suggesting that shape transformation to nanofibers could elevate cellular uptake. It is reported that some slender materials, such as nanofibers, nanorods, and nanoworms, etc., can increase cell adhesion and other functions through their large specific surface area, thus promoting cell uptake⁵⁶. When combined with iRGD, the amount of NPs swallowed by 4T1 cells after irradiation was 2.08 times as much as that by NPs alone, and was much higher than that of non-irradiation group. Introducing of iRGD indeed enhanced the cellular uptake of the transformable nanoparticles, which could be credited to the homing of iRGD to 4T1 cells through the $\alpha v\beta 3$ receptor⁵⁷. iRGD could trigger the endocytic bulk transport pathway by NRP-1-mediated “bystander effect”⁵⁸. Thus, the difference of the signal distribution indicated that the uptake of these nanoparticles was mainly related to endocytic pathway and iRGD could enhance the uptake. These results suggested that the combination strategy of PDT and iRGD

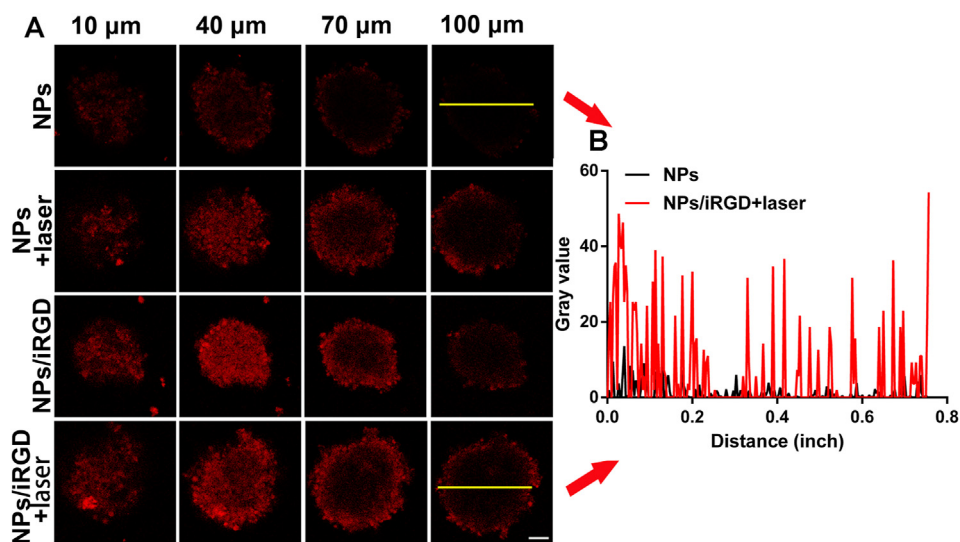


Figure 3 Penetration and retention in multicellular spheroid. (A) Penetration of NPs and NPs/iRGD upon or not upon 650 nm irradiation for 4 h by confocal microscopy, scale bar = 100 μm ; (B) Quantitative analyses of tumor spheroid sections at 100 μm .

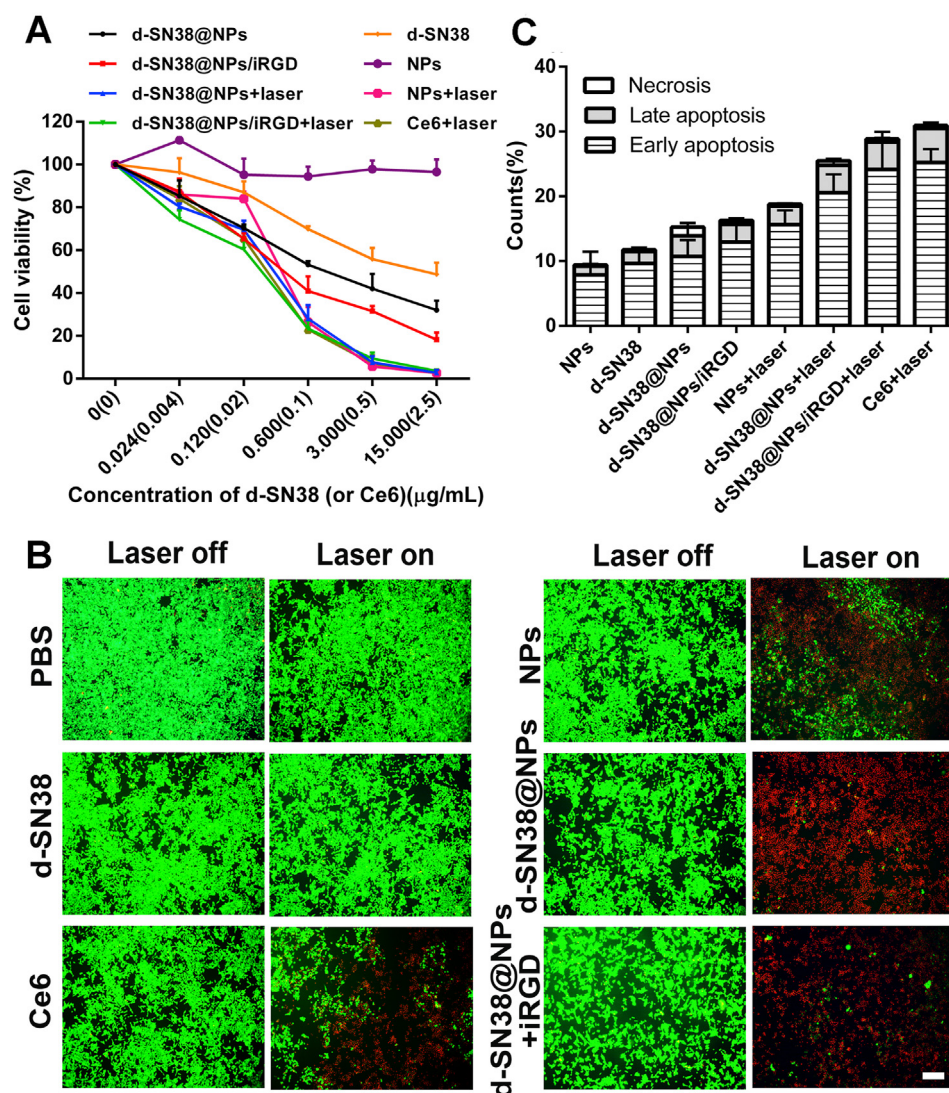


Figure 4 *In vitro* cytotoxicity studies of 4T1 cells incubated with different formulations. (A) Cell viability by MTT assay ($n = 3$); (B) Fluorescence images of calcein AM/PI double stain assay, scale bar = 50 μm ; (C) Apoptosis analysis by flow cytometry ($n = 3$).

was able to synergistically facilitate the penetration of the shape-transformable formulations.

3.5. Penetration and retention in multicellular spheroid

To confirm whether the shape change nanoparticles co-administrated with iRGD further enhanced penetration and retention in tumors, multicellular spheroids were prepared to simulate the tumor tissue. After 4 h incubation, due to the small particles size, all tested formulations distributed more than 40 μm of Z-axis to the tumor spheroid (Fig. 3A). Among them, NPs/iRGD+laser-treated spheroid maintained the strongest signal, which is about 1.69-fold of that without iRGD, even 2.93-fold of that of simple NPs (Supporting Information Fig. S6). Although the signal weakened as the depths deepened, enhanced signal could be clearly observed at 100 μm in NPs/iRGD+laser treated spheroid, while the signal of NPs tended to vanish. Corresponding quantify analysis of tumor spheroid sections at 100 μm was also consistent with this result (Fig. 3B and Fig. S6). Collectively, these results showed that the combination of PDT with iRGD could indeed

accelerate the accumulation of shape changeable nanoparticles into deep region of solid tumor. The study well demonstrated that with the help of iRGD, spherical NPs/iRGD could first penetrate in tumor by initially binding with $\alpha\text{v}\beta 3$ integrin receptors. And upon irradiation, the spherical NPs transformed into nanofibers, which were hard to be pumped back and thereby improved retention of NPs in the spheroids.

3.6. Cytotoxicity study

The enhanced cellular uptake prompted by combining PDT with iRGD paved the way for further systematically cytotoxicity evaluation of d-SN38@NPs/iRGD+laser. First, the relationship between *in vitro* cytotoxicity and incubation concentration of the prepared formulations was measured by MTT assay. The cytotoxicity of iRGD was evaluated, and it showed that iRGD almost has no cytotoxicity to cells at the tested concentrations of 0–100 $\mu\text{g}/\text{mL}$ (Supporting Information Fig. S7). Then, we measured the cytotoxicity of NPs to determine if the nanoparticle themselves caused any cytotoxicity. The results indicated that NPs

almost had no toxic effect on 4T1 cells even at the highest concentration (Fig. 4A). Whereas, when the concentration of Ce6 was more than 0.02 $\mu\text{g}/\text{mL}$, the irradiated NPs showed obvious cytotoxicity. When come to the irradiated free Ce6 group, the working concentration was much lower than that in irradiated NPs with an IC_{50} of 0.03 $\mu\text{g}/\text{mL}$. This result can be attributed to the generation of ROS, resulting in BR transformation. Compared to d-SN38, the nanoparticle formulations were more toxic to 4T1 cells. With the assistance of iRGD, d-SN38@NPs/iRGD (IC_{50} of 0.48 $\mu\text{g}/\text{mL}$) displayed an enhanced cytotoxic activity compared with d-SN38@NPs (IC_{50} of 1.33 $\mu\text{g}/\text{mL}$). Notably, post irradiation, when the concentration of d-SN38 was less than 0.6 $\mu\text{g}/\text{mL}$, d-SN38@NPs/iRGD+laser showed the strongest cytotoxicity compared with other preparations; while at higher concentrations, the cell viability of d-SN38@NPs or d-SN38@NPs/iRGD upon irradiation became comparable less than 10% owing to the synergy of chemotherapy and PDT.

Subsequently, dead-live staining assay was employed to directly observe the antitumor effect at cellular level. With or without irradiation, almost all the cells were alive in PBS group (Fig. 4B). In parallel, no obvious difference was observed in d-SN38 group. Whilst upon irradiation, Ce6 and NPs induced substantial cell death and displayed comparable vitalities at the detection concentration in line with the results of MTT assay. When treated with d-SN38@NPs and d-SN38@NPs/iRGD, nearly all the cells were died after irradiation, which further confirmed the synergistic effect of chemotherapy and PDT.

In addition, similar results were obtained with regard to apoptosis. After introducing a lower concentration of d-SN38 (0.25 $\mu\text{g}/\text{mL}$), the early and late apoptosis percentage of 4T1 cells treated with d-SN38@NPs/iRGD were 12.93% and 2.76%, which were higher than those of d-SN38 (9.66%, 1.82%) and d-SN38@NPs (10.71%, 3.23%; Fig. 4C). On the other hand, all the irradiation groups showed better apoptosis-inducing ability than non-irradiation groups. d-SN38@NPs/iRGD+laser induced 28.4% of cells in apoptotic stage, which was 1.15-fold higher than

that of d-SN38@NPs+laser (24.77%). These data further proved that combination of PDT and iRGD could give assistance to the uptake of d-SN38@NPs/iRGD+laser, which lead to more apoptosis compared with control nanoparticles.

3.7. Wound healing assay

To explore the inhibition effect of d-SN38@NPs/iRGD+laser for tumor cell motility, wound healing assay was performed. The results showed that laser irradiation can effectively promote inhibitory capability of the formulations in 4T1 cells (Fig. 5A and B). Remarkably, d-SN38@NPs/iRGD+laser-treated cells displayed the weakest healing ability at 24 h after scratching. Upon irradiation, the d-SN38@NPs/iRGD treatment reduced the wound healing rate to $2.51 \pm 1.44\%$, which was 3.25-fold lower than that of the d-SN38@NPs treated group, indicating the inhibitory effect of d-SN38@NPs was further strengthened by co-administration of iRGD. This enhanced inhibition capability may originate from (1) the *in situ* transformation of the nanoparticles into fibrils to construct artificial extracellular matrix, which was critical to the motility of metastatic cells¹⁶; and (2) the blockage of NPR receptors of cancer cells by iRGD, which induced partial cell detachment and collapse of cellular processes⁵⁹.

3.8. In vivo targeting efficiency

Ideally, the co-injection of d-SN38@NPs and iRGD is expected to improve the tumor targeting and therapeutic effect. Before the chemo-photodynamic therapy, pharmacokinetic profiles of d-SN38@NPs and d-SN38@NPs/iRGD were tested after a single intravenous injection in mice. As shown in Supporting Information Fig. S8 and Table S1, both d-SN38@NPs and d-SN38@NPs/iRGD have a long blood circulation half-life ($t_{1/2z}$), which was longer than 15 h. The mean residence time ($\text{MRT}_{0-\infty}$) for d-SN38@NPs/iRGD was 25.97 ± 8.75 h, which was 1.21-fold higher than that of d-SN38@NPs group. The result suggested that the prepared

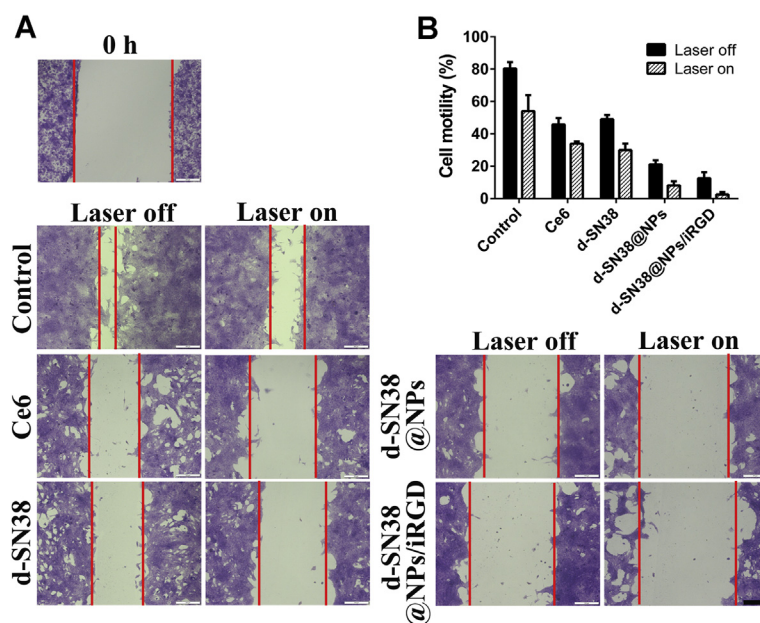


Figure 5 Wound healing assay of 4T1 cells incubated with different formulations. (A) Microscopy images and (B) quantitative analysis of wound healing, scale bar = 200 μm ($n = 3$).

vehicles could circulate for a long time in circulatory system and co-administration iRGD with d-SN38@NPs could prolong the blood retention time to a certain extent, which were beneficial to tumor targeting.

Then, the tumor targeting and penetration efficiency of d-SN38@NPs/iRGD+laser *in vivo* were validated in 4T1 mice model. At 24 h post injection, all the tested formulations showed stronger distribution at the tumor site than 4 h (Fig. 6A). d-SN38@NPs/iRGD irrespective of irradiation showed extensive signal in the whole body, suggesting that the enhanced circulating comparing with d-SN38@NPs, which was consistent with the results of pharmacokinetic experiments. On the other hand, d-SN38@NPs/iRGD-treated group demonstrated that the iRGD endorsed more nanoparticles accumulation than d-SN38@NPs, evidenced by stronger fluorescent signal in tumor. Importantly,

upon irradiation, d-SN38@NPs/iRGD displayed the strongest fluorescent intensity than laser off nanoparticles and d-SN38@NPs, supporting the notions that both iRGD and *in situ* nanoparticle-to-nanofiber transformation elevated tumor retention ability. The results were further confirmed by *ex vivo* imaging and the confocal imaging of sectioned organs and tumors (Fig. 6B–D). In consistent with the results of *in vivo* imaging at 24 h, the semi-quantification of *ex vivo* imaging showed d-SN38@NPs/iRGD with irradiation significantly accumulated 1.79-fold ($P < 0.001$) and 1.52-fold ($P < 0.01$) more in tumor when compared with d-SN38@NPs and d-SN38@NPs/iRGD without irradiation, respectively. The heavily accumulation at the liver of all formulations indicated they were cleared faster in liver than other organs. Similarly, confocal imaging of sectioned organs and tumors showed that the fluorescent intensity of

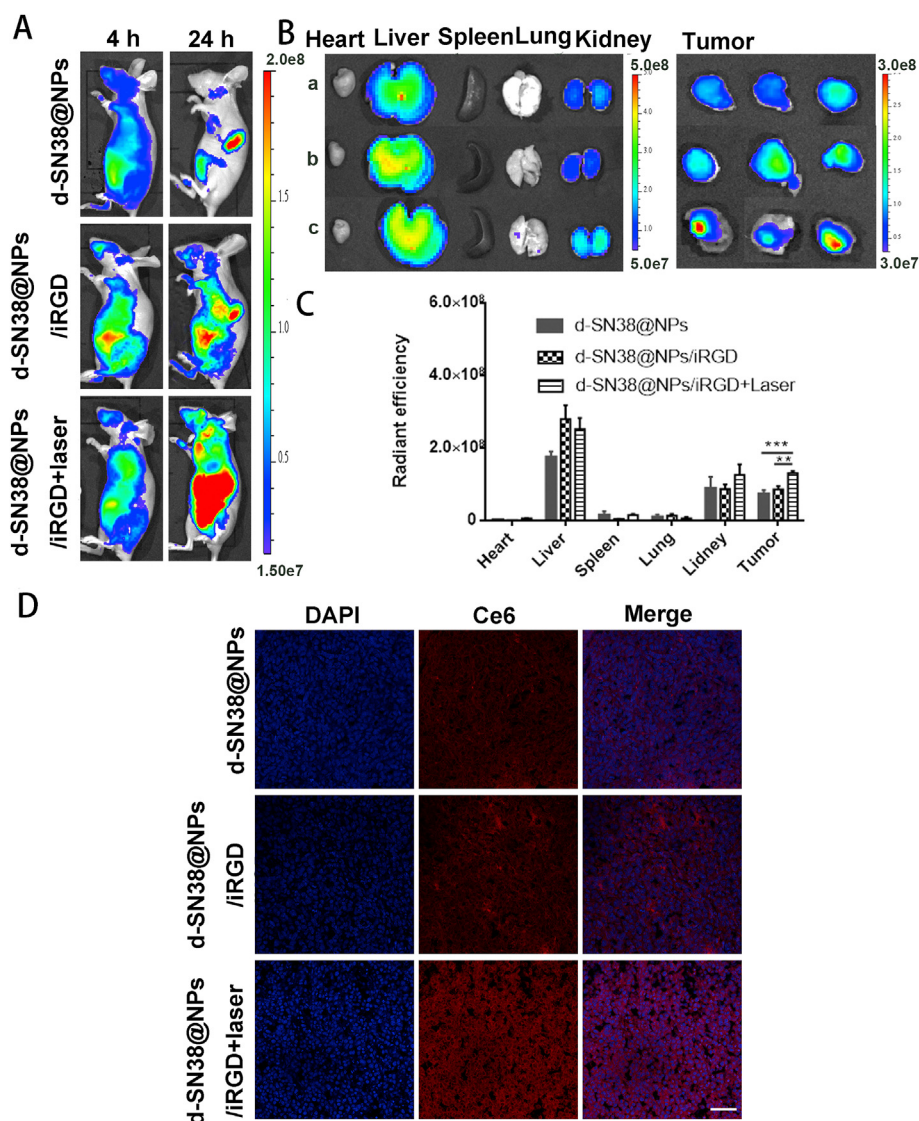


Figure 6 *In vivo* targeting efficiency of different formulations in 4T1 tumor-bearing mice. (A) Representative *in vivo* fluorescent imaging of mice from different groups at 4 and 24 h post injection; (B) *Ex vivo* fluorescence distribution imaging of major organs and tumors at 24 h after tail injection; (C) The semi-quantification of major organs and tumors at 24 h post injection ($n = 3$); (D) Fluorescence distribution in frozen sections of tumor tissue at 24 h after tail injection. The unit of color scales and radiant efficiency is [$\text{p s cm}^2/\text{sr}$]/[$\mu\text{W}/\text{cm}^2$]; In (B), a, b, c denotes d-SN38@NPs, d-SN38@NPs/iRGD, and d-SN38@NPs/iRGD+laser, respectively; $**P < 0.01$ and $***P < 0.001$; The bar in (D) represents 50 μm .

d-SN38@NPs/iRGD without irradiation was 1.46-fold higher than that of d-SN38@NPs, while the fluorescent intensity of d-SN38@NPs/iRGD with irradiation was the strongest, which was 1.94- and 1.33-fold higher than that of d-SN38@NPs and d-SN38@NPs/iRGD, respectively (Supporting Information Figs. S9 and S10). These results collectively suggested that presence of iRGD and the laser triggered shape transformation could effectively improve the targeting and penetration of nanoparticles to tumor parenchyma.

3.9. *In vivo* antitumor efficacy

Encouraged by the superior tumor penetration and distribution effect of chemotherapy/PDT combination strategy of d-SN38@NPs/iRGD, *in vivo* antitumor study was carried out using 4T1 tumor-bearing

mice. Compared to the rapid tumor growth curves of PBS, the groups receiving treatments all displayed a relatively slower growth rate. As shown in Fig. 7A, d-SN38@NPs group exhibited a moderate antitumor efficiency down to the monotherapy without laser. However, co-administration of iRGD with d-SN38@NPs apparently enhanced the inhibition efficiency with an inhibition rate of 30.55% on Day 18. When further combined with PDT, d-SN38@NPs/iRGD exhibited the strongest antitumor responsiveness with a tumor inhibition rate of 60.89%, which was 7.42-fold higher than simple d-SN38@NPs. In corresponding, the tumor weights of d-SN38@NPs/iRGD +laser were the lightest (Fig. 7B). In addition, the slightly body weight growth curve (Supporting Information Fig. S11) and histological images without obvious changes in the major organs (Supporting Information Fig. S12) collectively revealed that all treatments had satisfactory biocompatibility. This best

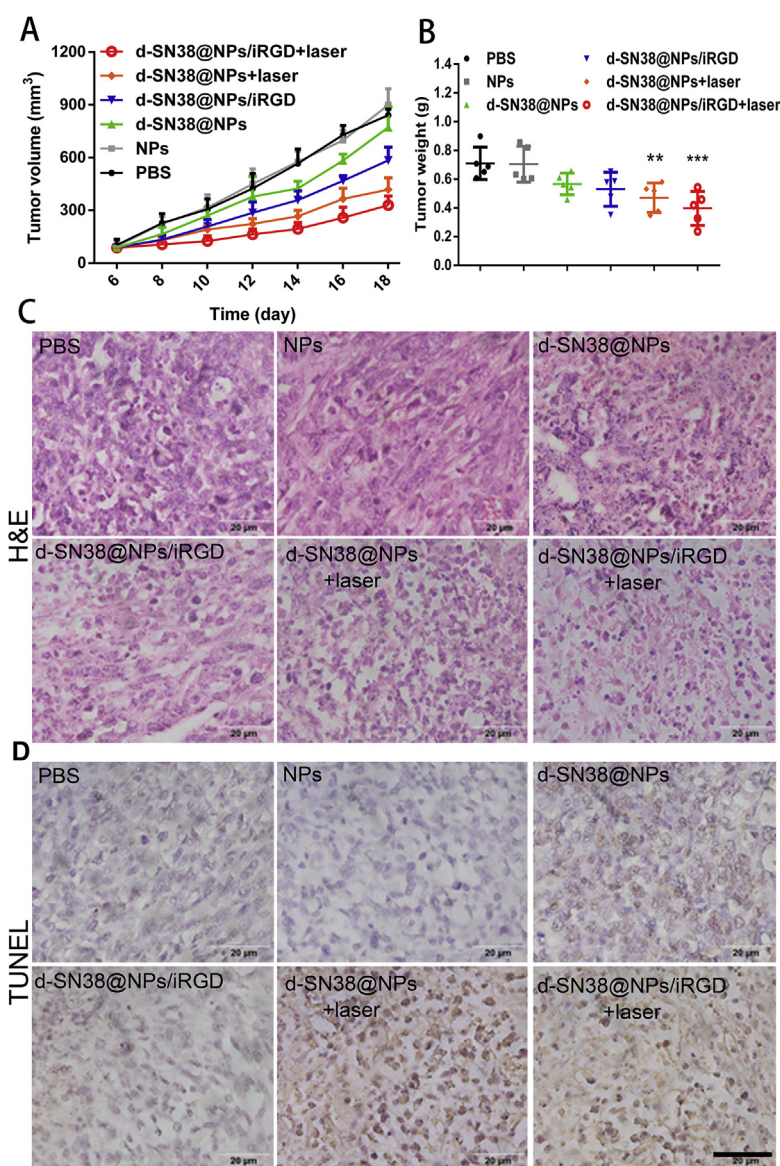


Figure 7 *In vivo* antitumor efficacy. (A) Tumor volume and (B) tumor weight of 4T1 tumor-bearing mice administered with PBS, NPs, d-SN38@NPs, d-SN38@NPs/iRGD, d-SN38@NPs+laser and d-SN38@NPs/iRGD+laser by intravenous injection, * $P < 0.05$, ** $P < 0.01$ and *** $P < 0.001$; Representative photographic image of (C) H&E staining and (D) TUNEL staining images of tumor tissues, scale bar = 20 μm .

performance of d-SN38@NPs/iRGD +laser could be put down to (1) the active targeting capacity of iRGD, which led to more nanoparticles homed to the tumor site; (2) the structural transformation of the formulation, resulting in an enhanced retention; (3) the synergistic effects by a combination of chemotherapy and PDT.

3.10. Immunohistochemistry analysis

To explore the underlying mechanism that enabled enhanced therapeutic efficacy, H&E staining and TUNEL staining assay were employed (Fig. 7C and D). In PBS and NPs groups, typical features of tumor cells with large and irregular nuclei were observed. On the contrary, d-SN38-loaded nanoparticle formulations presented fewer complete tumor shape and more apoptotic bodies. Strikingly, d-SN38@NPs/iRGD +laser showed the lowest density of live tumor cells, and the most apoptotic and necrotic cells than all the other examined formulations, confirming the improved tumor inhibition efficiency with the help of PDT and iRGD.

4. Conclusions

In this study, we set forth a stepwise stimuli-responsive strategy in which we co-administrated tumor penetration peptide iRGD with structural transformable nanoparticles to enhance tumor targeting, penetration and retention. d-SN38@NPs combined with iRGD could home to tumors after intravenous administration and penetrate into the deep region of tumor sites. Then laser responsiveness of the Ce6 component could not only release ROS upon laser irradiation, but also stimulate the gathered nanoparticles transformed into nanofibers at the tumor sites. Subsequently, the released d-SN38 inside the tumor cell responded to the high level of GSH, resulting in a high antitumor effect in 4T1 tumor-bearing mice due to the enhanced chemo-photodynamic therapy effect. Collectively, the results of this study demonstrate the potential of combination iRGD with transformable nanomedicines for enhancing chemo-photodynamic therapy against cancer.

Acknowledgments

The authors gratefully acknowledge the financial support from National Natural Science Foundation of China (Nos. 81961138009; 82071915), Research Funds of Sichuan Science and Technology Department (No.19YYJC2250, China), 111 Project (No. B18035, China), Fundamental Research Funds for the Central Universities, and Natural Science Foundation of Heilongjiang Province of China (No. YQ2019H004). We would be grateful to Dr. Chenghui Li (Analytical & Testing Center, Sichuan University, China) for her technical help.

Author contributions

Huile Gao and Xiangrong Yu designed the research. Congcong Lin and Fan Tong carried out the experiments and performed data analysis. Rui Liu, Rou Xie, Ting Lei, Yuxiu Chen and Zhihang Yang participated part of the experiments. Congcong Lin wrote and revised the manuscript. All of the authors have read and approved the final manuscript.

Conflicts of interest

The authors have no conflict of interest to declare.

Appendix A. Supporting information

Supporting data to this article can be found online at <https://doi.org/10.1016/j.apsb.2020.10.009>.

References

- Shi J, Kantoff PW, Wooster R, Farokhzad OC. Cancer nanomedicine: progress, challenges and opportunities. *Nat Rev Cancer* 2017;**17**:20–37.
- Danhier F. To exploit the tumor microenvironment: since the EPR effect fails in the clinic, what is the future of nanomedicine?. *J Control Release* 2016;**244**:108–21.
- Perry JL, Reuter KG, Luft JC, Pecot CV, Zamboni W, DeSimone JM. Mediating passive tumor accumulation through particle size, tumor type, and location. *Nano Lett* 2017;**17**:2879–86.
- Li C, Wang JC, Wang YG, Gao HL, Wei G, Huang YZ, et al. Recent progress in drug delivery. *Acta Pharm Sin B* 2019;**9**:1145–62.
- Sykes EA, Chen J, Zheng G, Chan WC. Investigating the impact of nanoparticle size on active and passive tumor targeting efficiency. *ACS Nano* 2014;**8**:5696–706.
- Hickey JW, Santos JL, Williford JM, Mao HQ. Control of polymeric nanoparticle size to improve therapeutic delivery. *J Control Release* 2015;**219**:536–47.
- Shao D, Lu MM, Zhao YW, Zhang F, Tan YF, Zheng X, et al. The shape effect of magnetic mesoporous silica nanoparticles on endocytosis, biocompatibility and biodistribution. *Acta Biomater* 2017;**49**:531–40.
- Yu WQ, Shevtsov M, Chen XC, Gao HL. Advances in aggregatable nanoparticles for tumor-targeted drug delivery. *Chin Chem Lett* 2020;**31**:1366–74.
- Tang L, Yang XJ, Yin Q, Cai KM, Wang H, Chaudhury I, et al. Investigating the optimal size of anticancer nanomedicine. *Proc Natl Acad Sci U S A* 2014;**111**:15344–9.
- Kibria G, Hatakeyama H, Ohga N, Hida K, Harashima H. The effect of liposomal size on the targeted delivery of doxorubicin to Integrin $\alpha v\beta 3$ -expressing tumor endothelial cells. *Biomaterials* 2013;**34**:5617–27.
- Hu C, Cun XL, Ruan SB, Liu R, Xiao W, Yang XT, et al. Enzyme-triggered size shrink and laser-enhanced NO release nanoparticles for deep tumor penetration and combination therapy. *Biomaterials* 2018;**168**:64–75.
- Ruan SB, He Q, Gao HL. Matrix metalloproteinase triggered size-shrinkable gelatin-gold fabricated nanoparticles for tumor microenvironment sensitive penetration and diagnosis of glioma. *Nanoscale* 2015;**7**:9487–96.
- Ruan S, Cao X, Cun XL, Hu GL, Zhou Y, Zhang YJ, et al. Matrix metalloproteinase-sensitive size-shrinkable nanoparticles for deep tumor penetration and pH triggered doxorubicin release. *Biomaterials* 2015;**60**:100–10.
- Yu WQ, Liu R, Zhou Y, Gao HL. Size-tunable strategies for a tumor targeted drug delivery system. *ACS Cent Sci* 2020;**6**:100–16.
- Zhong L, Xu L, Liu YY, Li QS, Zhao DY, Li ZB, et al. Transformative hyaluronic acid-based active targeting supramolecular nanoplatform improves long circulation and enhances cellular uptake in cancer therapy. *Acta Pharm Sin B* 2019;**9**:397–409.
- Hu XX, He PP, Qi GB, Gao YJ, Lin YX, Yang C, et al. Transformable nanomaterials as an artificial extracellular matrix for inhibiting tumor invasion and metastasis. *ACS Nano* 2017;**11**:4086–96.

17. Bellat V, Ting R, Southard TL, Vahdat L, Molina H, Fernandez J, et al. Functional peptide nanofibers with unique tumor targeting and enzyme-induced local retention properties. *Adv Funct Mater* 2018;**28**:1803969.
18. Liu R, Yu MN, Yang XT, Umeshappa CS, Hu C, Yu WQ, et al. Linear chimeric triblock molecules self-assembled micelles with controllably transformable property to enhance tumor retention for chemo-photodynamic therapy of breast cancer. *Adv Funct Mater* 2019;**29**:1808462.
19. Wang Y, Wei GY, Zhang XB, Xu FN, Xiong X, Zhou SB. A step-by-step multiple stimuli-responsive nanoplatfor for enhancing combined chemo-photodynamic therapy. *Adv Mater* 2017;**29**:201605357.
20. Lee Y, Lee S, Lee DY, Yu B, Miao W, Jon S. Multistimuli-responsive bilirubin nanoparticles for anticancer therapy. *Angew Chem Int Ed Engl* 2016;**55**:10676–80.
21. Qian CG, Yu JC, Chen YL, Hu QY, Xiao XZ, Sun WJ, et al. Light-activated hypoxia-responsive nanocarriers for enhanced anticancer therapy. *Adv Mater* 2016;**28**:3313–20.
22. Anchordoquy TJ, Barenholz Y, Boraschi D, Chorny M, Decuzzi P, Dobrovolskaia MA, et al. Mechanisms and barriers in cancer nanomedicine: addressing challenges, looking for solutions. *ACS Nano* 2017;**11**:12–8.
23. Liu R, An Y, Jia WF, Wang YS, Wu Y, Zhen YH, et al. Macrophage-mimic shape changeable nanomedicine retained in tumor for multimodal therapy of breast cancer. *J Control Release* 2020;**321**:589–601.
24. Yu WQ, He XQ, Yang ZH, Yang XT, Xiao W, Liu R, et al. Sequentially responsive biomimetic nanoparticles with optimal size in combination with checkpoint blockade for cascade synergetic treatment of breast cancer and lung metastasis. *Biomaterials* 2019;**217**:119309.
25. Yang L, Gao P, Huang Y, Lu X, Chang Q, Pan W, et al. Boosting the photodynamic therapy efficiency with a mitochondria-targeted nanophotosensitizer. *Chin Chem Lett* 2019;**30**:1293–6.
26. Jiang Q, Liu Y, Guo RR, Yao XX, Yang W. Erythrocyte-cancer hybrid membrane-camouflaged melanin nanoparticles for enhancing photothermal therapy efficacy in tumors. *Biomaterials* 2018;**192**:292–308.
27. Pei Q, Hu XL, Zheng XH, Liu S, Li Y, Jing XB, et al. Light-activatable red blood cell membrane-camouflaged dimeric prodrug nanoparticles for synergistic photodynamic/chemotherapy. *ACS Nano* 2018;**12**:1630–41.
28. He X, Cai KM, Zhang Y, Lu YF, Guo Q, Zhang YJ, et al. Dimeric prodrug self-delivery nanoparticles with enhanced drug loading and bioreduction responsiveness for targeted cancer therapy. *ACS Appl Mater Interfaces* 2018;**10**:39455–67.
29. Song Y, Li D, He JL, Zhang MZ, Ni PH. Facile preparation of pH-responsive PEGylated prodrugs for activated intracellular drug delivery. *Chin Chem Lett* 2019;**30**:2027–31.
30. Zheng P, Liu Y, Chen JJ, Xu WG, Li G, Ding JX. Targeted pH-responsive polyion complex micelle for controlled intracellular drug delivery. *Chin Chem Lett* 2020;**31**:1178–82.
31. Yang X, Hu C, Tong F, Liu R, Zhou Y, Qin L, et al. Tumor microenvironment-responsive dual drug dimer-loaded pegylated bilirubin nanoparticles for improved drug delivery and enhanced immune-chemotherapy of breast cancer. *Adv Funct Mater* 2019;**29**:1901896.
32. Wang HX, Chen JM, Xu C, Shi LL, Tayier M, Zhou JH, et al. Cancer nanomedicines stabilized by π - π stacking between heterodimeric prodrugs enable exceptionally high drug loading capacity and safer delivery of drug combinations. *Theranostics* 2017;**7**:3638.
33. Bala V, Rao S, Boyd BJ, Prestidge CA. Prodrug and nanomedicine approaches for the delivery of the camptothecin analogue SN38. *J Control Release* 2013;**172**:48–61.
34. Guo Q, Luo P, Luo Y, Du F, Lu W, Liu SY, et al. Fabrication of biodegradable micelles with sheddable poly(ethylene glycol) shells as the carrier of 7-ethyl-10-hydroxy-camptothecin. *Colloids Surf B Biointerfaces* 2012;**100**:138–45.
35. Fujiwara Y, Minami H. An overview of the recent progress in irinotecan pharmacogenetics. *Pharmacogenomics* 2010;**11**:391–406.
36. Takakura A, Kurita A, Asahara T, Yokoba M, Yamamoto M, Ryuge S, et al. Rapid deconjugation of SN-38 glucuronide and adsorption of released free SN-38 by intestinal microorganisms in rat. *Oncol Lett* 2012;**3**:520–4.
37. Wang CC, Liu LC, Cao HL, Zhang WA. Intracellular GSH-activated galactoside photosensitizers for targeted photodynamic therapy and chemotherapy. *Biomater Sci* 2017;**5**:274–84.
38. Such GK, Yan Y, Johnston AP, Gunawan ST, Caruso F. Interfacing materials science and biology for drug carrier design. *Adv Mater* 2015;**27**:2278–97.
39. Ruan SB, Xiao W, Hu C, Zhang HJ, Rao JD, Wang SH, et al. Ligand-mediated and enzyme-directed precise targeting and retention for the enhanced treatment of glioblastoma. *ACS Appl Mater Interfaces* 2017;**9**:20348–60.
40. Hu C, Yang XT, Liu R, Ruan SB, Zhou Y, Xiao W, et al. Coadministration of iRGD with multistage responsive nanoparticles enhanced tumor targeting and penetration abilities for breast cancer Therapy. *ACS Appl Mater Interfaces* 2018;**10**:22571–9.
41. Desgrosellier JS, Cheresch DA. Integrins in cancer: biological implications and therapeutic opportunities. *Nat Rev Cancer* 2010;**10**:9–22.
42. Teesalu T, Sugahara KN, Kotamraju VR, Ruoslahti E. C-end rule peptides mediate neuropilin-1-dependent cell, vascular, and tissue penetration. *Proc Natl Acad Sci U S A* 2009;**106**:16157–62.
43. Sugahara KN, Teesalu T, Karmali PP, Kotamraju VR, Agemy L, Greenwald DR, et al. Coadministration of a tumor-penetrating peptide enhances the efficacy of cancer drugs. *Science* 2010;**328**:1031–5.
44. Liu R, Xiao W, Hu C, Xie R, Gao HL. Theranostic size-reducible and no donor conjugated gold nanocluster fabricated hyaluronic acid nanoparticle with optimal size for combinational treatment of breast cancer and lung metastasis. *J Control Release* 2018;**278**:127–39.
45. Zhang X, Lin CC, Lu AP, Lin G, Chen HJ, Liu Q, et al. Liposomes equipped with cell penetrating peptide BR2 enhances chemotherapeutic effects of cantharidin against hepatocellular carcinoma. *Drug Deliv* 2017;**24**:986–98.
46. Lin CC, Zhang X, Chen HB, Bian ZX, Zhang G, Riaz MK, et al. Dual-ligand modified liposomes provide effective local targeted delivery of lung-cancer drug by antibody and tumor lineage-homing cell-penetrating peptide. *Drug Deliv* 2018;**25**:256–66.
47. Chereddy KK, Her C-H, Comune M, Moia C, Lopes A, Porporato PE, et al. PLGA nanoparticles loaded with host defense peptide LL37 promote wound healing. *J Control Release* 2014;**194**:138–47.
48. Cun XL, Chen JT, Ruan SB, Zhang L, Wan JY, He Q, et al. A novel strategy through combining iRGD peptide with tumor-microenvironment-responsive and multistage nanoparticles for deep tumor penetration. *ACS Appl Mater Interfaces* 2015;**7**:27458–66.
49. Guo Y, Jiang K, Shen ZC, Zheng GR, Fan LL, Zhao RR, et al. A small molecule nanodrug by self-assembly of dual anticancer drugs and photosensitizer for synergistic near-infrared cancer theranostics. *ACS Appl Mater Interfaces* 2017;**9**:43508–19.
50. Khodadadei F, Safarian S, Ghanbari N. Methotrexate-loaded nitrogen-doped graphene quantum dots nanocarriers as an efficient anticancer drug delivery system. *Mater Sci Eng C Mater Biol Appl* 2017;**79**:280–5.
51. Mo R, Gu Z. Tumor microenvironment and intracellular signal-activated nanomaterials for anticancer drug delivery. *Mater Today* 2016;**19**:274–83.
52. Cai KM, He X, Song ZY, Yin Q, Zhang YF, Uckun FM, et al. Dimeric drug polymeric nanoparticles with exceptionally high drug loading and quantitative loading efficiency. *J Am Chem Soc* 2015;**137**:3458–61.
53. Danhier F, Feron O, Préat V. To exploit the tumor microenvironment: passive and active tumor targeting of nanocarriers for anti-cancer drug delivery. *J Control Release* 2010;**148**:135–46.
54. Pang HB, Braun GB, She ZG, Kotamraju VR, Sugahara KN, Teesalu T, et al. A free cysteine prolongs the half-life of a homing

- peptide and improves its tumor-penetrating activity. *J Control Release* 2014;**175**:48–53.
55. Yang YY, Chen QL, Li SY, Ma W, Yao GY, Ren F, et al. iRGD-mediated and enzyme-induced precise targeting and retention of gold nanoparticles for the enhanced imaging and treatment of breast cancer. *J Biomed Nanotechnol* 2018;**14**:1396–408.
56. Shi J, Kantoff PW, Wooster R, Farokhzad OC. Cancer nanomedicine: progress, challenges and opportunities. *Nat Rev Cancer* 2017;**17**:20.
57. Cho HJ, Lee SJ, Park SJ, Paik CH, Lee SM, Kim S, et al. Activatable iRGD-based peptide monolith: targeting, internalization, and fluorescence activation for precise tumor imaging. *J Control Release* 2016;**237**:177–84.
58. Ruoslahti E. Peptides as targeting elements and tissue penetration devices for nanoparticles. *Adv Mater* 2012;**24**:3747–56.
59. Sugahara KN, Braun GB, de Mendoza TH, Kotamraju VR, French RP, Lowy AM, et al. Tumor-penetrating iRGD peptide inhibits metastasis. *Mol Cancer Ther* 2015;**14**:120–8.